Response of Thin Films and Substrate to Micro-Scale Laser Shock Peening

Youneng Wang
e-mail: yw2119@columbia.edu

Hongqiang Chen

Jeffrey W. Kysar

Y. Lawrence Yao

Department of Mechanical Engineering,
Columbia University,
New York, NY 10027

Micro-scale laser shock peening (μLSP) *can potentially be applied to metallic structures in microdevices to improve fatigue and reliability performance. Copper thin films on a single-crystal silicon substrate are treated by using* μLSP *and characterized using techniques of X-ray microdiffraction and electron backscatter diffraction (EBSD). Strain field, dislocation density, and microstructure changes including crystallographic texture, grain size and subgrain structure are determined and analyzed. Further, shock peened single crystal silicon was experimentally characterized to better understand its effects on thin films response to* μLSP. *The experimental result is favorably compared with finite element method simulation based on single-crystal plasticity.* [DOI: 10.1115/1.2714568]

1 Introduction

The reliability and failure of micro-electromechanical system (MEMS) are of concern for long-term applications and efforts have made on these aspects over the last few years [1,2]. MEMS devices like switches and gears experience cyclic loads in applications, and actuators fail because of wear and friction of the rubbing surface [3]. Silicon is the most dominant material in MEMS devices, but metals such as aluminum, copper, gold, and nickel are often used in MEMS as electrical conductors and occasionally as a structural material due to its high electric conductivity and ease of use. When metals are used, for example thin film microwave switches, they are usually deposited as a film over a substrate, which is usually single-crystal silicon. Consequently, improvement of reliability and fatigue performance of metallic thin film have been the subject of much research.

Laser shock peening (LSP) produces a compressive residual stress in the surface of metallic materials, which significantly increases fatigue life and wear resistance in applications [4–6]. Compared with shot peening, the compressive stresses extend much deeper below the surface and the resulting fatigue life enhancement is significant [4]. Increases in hardness and tensile strength are also observed [5,7].

Microscale laser shock peening (μLSP) is a technique in which LSP is implemented using a laser beam of micron length scale. It can potentially be applied to manipulate the residual stress distribution in surface layers of metal structures with micron-level spatial resolution and thus enhance fatigue and reliability performances of microdevices [8]. It was found by using X-ray microdiffraction measurements that even a micron sized beam imparts appreciable compressive residual stress within bulk metals. Also, the response to μLSP for single crystal metals was numerically studied by finite element method (FEM) analysis [9].

However, it is more desirable to understand the response of metallic thin films to μLSP since most metal MEMS structures are made from metallic thin films. Zhang et al. [10,11] investigated the μLSP effects on a copper thin film on silicon substrate through average stress and hardness evaluation. It was seen from the average stress measurement that compressive residual stress was induced into thin films by μLSP similar to bulk metals but with a reduced magnitude. Though the work [10,11] gives some insights into the area, it is far from a complete understanding since there is no direct investigation of μLSP induced microstructural changes, such as crystallographic texture, grain, and subgrain structures, which mechanical properties of thin film are highly dependent on. Therefore, it is of great interest to quantitatively characterize and understand microstructure changes after μLSP. Also, response of thin films to μLSP is more or less affected by substrate on which they are deposited. Metallic microcomponents are normally made by patterning metallic films on a substrate and then sacrificing the substrate. Since μLSP needs to be applied between the two steps, it is definitely important to understand substrate response to μLSP in order to fully understand effects of μLSP to thin film on substrate.

In this paper, the μLSP-induced stress/strain in copper thin films was experimentally analyzed by the diffraction intensity contrast method, and the microstructure after μLSP was characterized by both X-ray microdiffraction and electron backscatter diffraction (EBSD). In addition, the silicon substrate after μLSP was investigated by X-ray microdiffraction. The experimental results for the substrate were then compared with that of simulations obtained from FEM analysis. These investigations provide groundwork for further numerical and theoretical analyses of response of the thin films with silicon substrate to μLSP.

2 Laser Shock Processing and Experiment Conditions

When a metallic target is irradiated by an intense (>1 GW/cm^2) laser pulse, the surface layer instantaneously vaporizes into a high pressure (1–10 GPa) plasma. This plasma induces shock waves during expansion from the irradiated surface, and mechanical impulses are transferred to the target. If the plasma is confined by water or other media, the shock pressure can be magnified by a factor of 5 or more compared with the open air condition [12]. These pressures are well above the yield stress of most metals, thus plastic deformation can be induced. As a result, if the peak shock pressure is over the Hugoniot elastic limit "HEL" of the target material for a suitable time duration, compressive stress distribution in the irradiated volume can be formed [4].

A frequency tripled Q-switched Nd:YAG laser ($\lambda = 355$ nm) in TEM_{00} mode was used in μLSP and the parameters of pulse duration, wavelength and beam diameter are shown in Fig. 1. A line of μLSP shocks was created on the sample surface with a 25 μm spacing. Pulse energies, 356 and 228 μJ, corresponding to laser intensities of 6.30 GW/cm^2 and 4.03 GW/cm^2, respectively, were used. A thin layer of high vacuum grease (about 10 μm thick) was spread evenly on the sample surface, and a 16-μm-thick polycrystalline aluminum foil, chosen for its relatively low threshold of

Contributed by the Manufacturing Engineering Division of ASME for publication in the Journal of Manufacturing Science and Engineering. Manuscript received November 22, 2004; final manuscript received November 10, 2006. Review conducted by Kamlakar Rajurkar. Paper presented at the 2004 International Congress on Applications of Lasers & Electro-Optics (ICALEO).

Copyright © 2007 by ASME

Downloaded 04 Jan 2008 to 128.59.149.201. Redistribution subject to ASME license or copyright; see http://www.asme.org/terms/Terms_Use.cfm

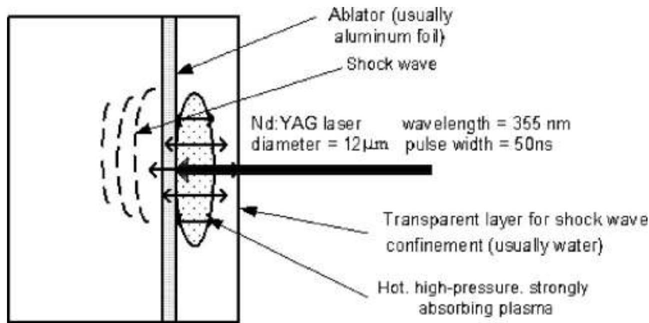

Fig. 1 Laser shock peening process

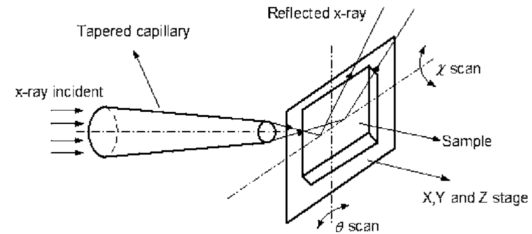

Fig. 3 Divergence of X-ray beam incident and θ, and χ scans of sample (distance from sample to the capillary tip is about 3 mm, the focused spot size is about 2 μm, the divergence angle is 0.6 deg, and the spot size on the sample surface is about 5 μm)

vaporization, was tightly pressed onto the grease. The sample was placed in a shallow container filled with distilled water around 3 mm above the sample's top surface. After shock processing, the coating layer and the vacuum grease were manually removed. The induced deformation is due to shock pressure and not due to thermal effects since only the coating is vaporized by the laser shocking [10].

The samples are copper thin films of 1 μm and 3 μm thickness on single crystal silicon wafer with (001) orientation. The 1 μm samples were prepared by physical vapor deposition (PVD) at a chamber pressure of 2 mTorr while the 3 μm samples were by electroplating process. It can be seen from X-ray diffraction result as shown in Fig. 2 that both 1 μm and 3 μm samples show strong (111) texture. In addition, silicon wafers with (001) orientation were used for shocking experiments as well. For Si samples, the shocked line is carefully aligned with the [110] direction. In this way, the active slip systems are confined approximately within the (110) plane which results in an approximate plane and symmetric deformation [10].

3 Measurement and Characterization Methods

3.1 X-Ray Microdiffraction Measurement. X-ray microdiffraction is a relatively new method in material characterization in micron scale resolution [13], which is required to characterize the samples treated by μLSP since the shocked area is usually in tens of microns [14]. In this case, high brightness synchrotron radiation sources are used for speed and accuracy in X-ray microdiffraction experiments at the beamline X20A of National Synchrotron Light Source (NSLS) in Brookhaven National Lab. The radiation energies for films and substrate are 8.0 keV (λ =1.54024 Å) and 8.5 keV (λ=1.458 Å), respectively, because copper films are less absorbent for the incident X-ray of 8.5 keV [15].

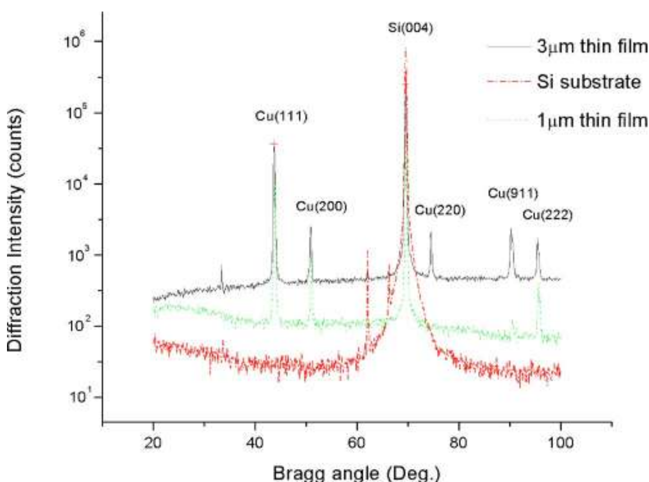

Fig. 2 Characterization of testing materials (1 μm and 3 μm Cu polycrystalline films on [004] single crystal Si substrate) by conventional X-ray diffraction

In the experiment, multiple points across the shock line were chosen for measurement. Spacing between adjacent measurement points is 5 μm within ±20 μm from the center of the shocked line and the spacing is 10 μm at greater distances in order to characterize the shocked area with micron scale resolution. Because the sample is not ideally parallel to each other and the incident X-ray beam is divergent, the X-ray incident must be realigned at each measurement position to satisfy Bragg angle condition. As shown in Fig. 3, the alignment angles χ and θ are optimized by scanning the diffracted intensity as a function of χ and θ, respectively, at each measurement location to achieve the highest diffracted intensity. Once the specimen orientation is properly set, the 2θ value of the peak can be measured by a detector scan in 2θ or by a radial scan where 2θ and θ are stepped at the symmetric 2:1 ratio. Also, in order to achieve the micron scale resolution, the X-ray incident spot size on the target should be as small as possible, which is related to the divergence angle and distance from tip to target as shown in Fig. 3. In this case, the spot size on target is 5 μm ×7 μm (along the shock line).

3.2 X-Ray Profile Evaluation Method by Fourier Transformation. The shock peening induces nonuniform strain and produces dislocation arrays, such as substructures or subgrains [9]. Both kinds of effects contribute to the broadening of the X-ray line profile in plastically deformed metals [16]. The Warren and Averbach method [17] based on the Fourier analysis of the diffraction profiles allows one to obtain the strain deviation and the distribution function of grain size directly from the Fourier series coefficients.

From the analysis in Ref. [17], the sample can be represented as columns of unit cells along the direction which are perpendicular to the diffraction plane. The X-ray line profile can be considered as the combination of reflected X-rays from all pairs of unit cells. The measured X-ray line profile is then represented as the Fourier series in reciprocal lattice space [17]

$$P(2\theta) = \frac{KNF^2}{\sin^2\theta} \sum_{n=-\infty}^{+\infty} (A_n \cos 2\pi nh + B_n \sin 2\pi nh) \tag{1}$$

where $P(2\theta)$ represents the measured X-ray line profile versus 2θ, F is the structure factor; K is the angular factor; N represents the number of unit cells in the sample; and h is the reciprocal of the lattice spacing. The real part of Fourier coefficient A_n can be described as the product of the size effect and the strain effect [17]

$$A_n = A_n^S A_n^D \tag{2}$$

where A_n^D represents the spacing change between the diffraction planes and A_n^S is a measure of the grain size. Furthermore, for small values of l and n, A_n can be expressed by [17]

Downloaded 04 Jan 2008 to 128.59.149.201. Redistribution subject to ASME license or copyright; see http://www.asme.org/terms/Terms_Use.cfm

$$\ln A_n = \ln A_n^S - 2\pi^2 l^2 n^2 \langle \varepsilon^2 \rangle \quad (3)$$

where l is the number of unit cells between diffraction planes and $\langle \varepsilon^2 \rangle^{1/2}$ is standard strain deviation which indicates strain uncertainty. According to Eq. (3), $\ln(A_n)$ versus n^2 is represented as a straight line, whose slope and intersection with $n=0$ can be used to evaluate the strain deviation and size effects.

Ungar [16] modified the *W-A* analysis of Fourier coefficients of X-ray profiles by taking into account the effect that a dislocation density has on the profiles. This procedure is known as the modified *W-A* analysis, and it enables a straightforward estimation of dislocation density from X-ray line profile analysis. For crystals containing dislocations, the diffraction profile is also considered as the combination of the diffracted X-ray for all unit cells in crystal as that in Warren's method. However, the displacement of each unit cell is represented by the dislocation Burgers vector to account for the effect of dislocation structure and the real part of the Fourier coefficients of the X-ray line profile can be written as [16]

$$\ln A_n = c_0 - \rho^* n^2 \ln(R_e/n) + Q^* n^4 \ln(R_2/n)\ln(R_3/n) \quad (4)$$

where ρ^* is the "formal" dislocation density, directly available from a broadened profile without taking into account the effect caused by different types of dislocations. Q^* is given as the variation of the dislocation density; n is the harmonic number; and R_e is the outer cutoff radius of dislocations, which indicates the distribution range of dislocation stored energy. R_2 and R_3 are auxiliary constants. The "true" or estimated value of dislocation density is

$$\rho = \frac{2\rho^*}{\pi g^2 b^2 \bar{C}} \quad (5)$$

where $\bar{C}$ is the average contrast factor for different type of dislocations (edge and screw) in the case of a particular *hkl* reflection and can be found in Ref. [16]; b is the Burgers vector of dislocations which is $a/2\langle 110\rangle$ here for FCC metals; and g is the diffraction vector. Thus, after calculating the real part of the Fourier coefficients A_n, the $\ln(A_n)$ versus n data can be fitted as a nonlinear curve using the formula in Eq. (3). The parameters such as ρ^* can be determined in curve fitting using the least-squares evaluation method and the dislocation density ρ can be estimated by Eq. (5).

3.3 EBSD Measurement. EBSD is used to examine a wide range of crystalline materials and to measure microstructure, orientation, texture, and boundary properties [18]. In this paper, the microstructure including texture, grain, and subgrain structures was studied for 1 μm film samples. CHANNEL5 EBSD system of HKL Technology was employed, which is attached to a JEOL JSM 5600LV scanning electron microscope. The shocked area was accurately located using scanning electron microscopy (SEM) before EBSD measurement by marking the shock line at several points during shock peening with three more pulses.

4 Results and Discussion

4.1 Characterization of Shocked Thin Films via X-Ray Microdiffraction Analysis. In this subsection, the recorded X-ray profiles for the thin films were analyzed by Fourier transformation and the corresponding results such as strain deviation, grain size, and dislocation density were discussed.

4.1.1 Strain Field by the Intensity Contrast Method. After applying μLSP, the stress/strain in the thin film is coupled to and deforms the substrate. Imperfections such as small grain blocks or subgrains are induced into the substrate under the shocked film. The blocks are regions of crystal misorientation which are essentially nonparallel, which cause some of the extinction diffractions of the ideal crystal to become nonzero, resulting in an increase of

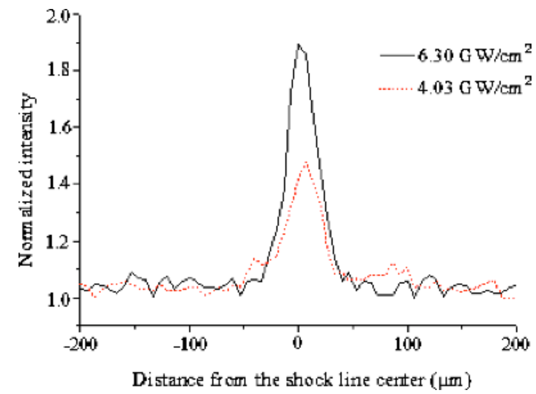

Fig. 4 Diffraction intensity contrast measurements across the shock line of 3 μm thin film under different energy levels

the reflecting diffraction intensity from the substrate in shocked region. Figure 4 shows the diffraction intensity contrast under two different laser energy levels for a 3 μm film sample. It can be seen that the μLSP effect is about ±25 μm around the shocked center and the intensity contrast increases markedly in the shocked region. Note that the diffraction contrast method gives only a qualitative measure of strain fields.

4.1.2 Strain Deviation, Grain Size, and Dislocation Density by Fourier Transformation. In order to better understand shock-induced plastic deformation, it is necessary to study the corresponding inhomogeneous strain variation in the depth direction, which can be calculated from the recorded X-ray profiles (Fig. 5) according to the method discussed in Sec. 3.2. From the theory of Ref. [17], for small values of l and n, the logarithm of the measured Fourier coefficient is given by Eq. (3). For (111) reflection, $l=3$, so the strain effect term can be represented as $-2\pi^2 l^2 n^2 \langle \varepsilon_l^2 \rangle$, in which $\langle \varepsilon_l^2 \rangle^{1/2}$ represented standard strain deviation caused by the laser shock peening in the $\langle 111\rangle$ direction. If we choose n^2 as the x axis and $\ln[A_n(l)]$ as the y axis, Eq. (3) represents a straight line with slope $K=-2\pi^2 l^2 \langle \varepsilon^2 \rangle$. Thus, the slope of this fitted line can be used to calculate the strain deviation $\langle \varepsilon_l^2 \rangle^{1/2} = \sqrt{K/-2\pi^2 l^2}$. X-ray profiles at each position cross the shocked line, from 40 μm left of the shocked line to 40 μm right, were processed by using Fourier transformation with Stoke's correction [19] based on $\ln A_n$ versus n^2 lines as shown in Fig. 6. Figure 7 shows the result of the

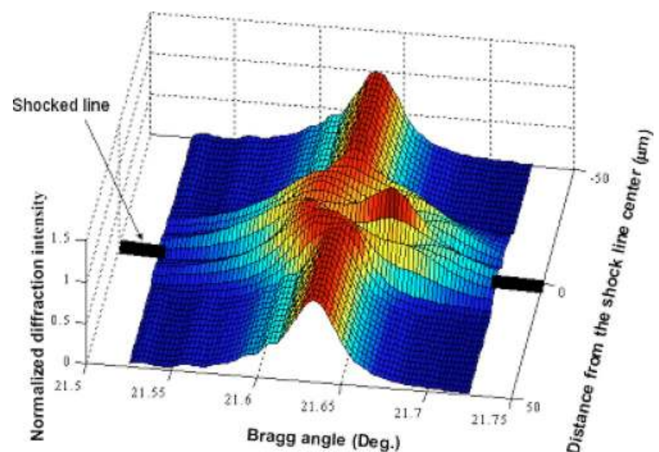

Fig. 5 3D X-ray profile spatial distribution across the shock line of 3 μm thin film (laser energy of 6.30 GW/cm^2, spatial resolution is 5 μm close to the line and 10 μm far away from the line)

Downloaded 04 Jan 2008 to 128.59.149.201. Redistribution subject to ASME license or copyright; see http://www.asme.org/terms/Terms_Use.cfm

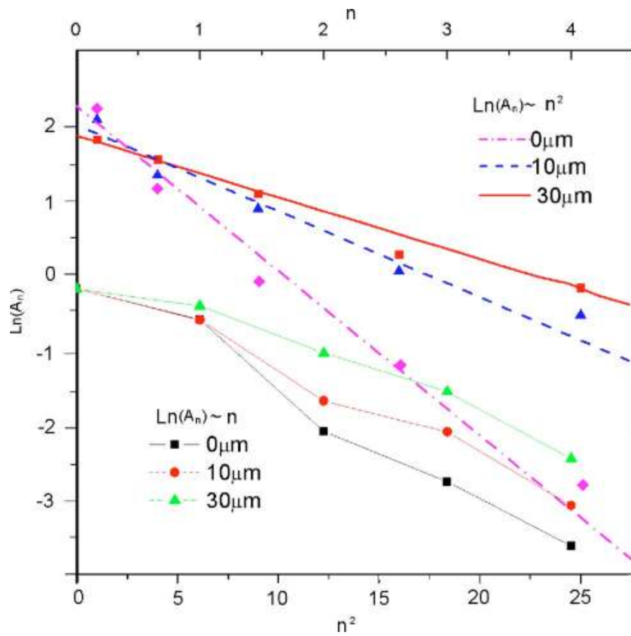

Fig. 6 ln(A_n) versus n^2 and ln(A_n) versus n lines at different positions from the center of shocked line (A_n: the real part of corrected Fourier coefficient; and n: Fourier series number)

spatial distribution of strain deviation in depth direction. It can be seen that the maximum deviation is about ±0.025 at the center and decreases to zero at around ±30 μm from the center, which strongly indicates that nonuniform strain is induced by laser shock peening. The result is consistent with that obtained from the intensity contrast method discussed above.

Dislocation cell structures were observed via transmission electron microscopy (TEM) in laser shock peened metals such as copper [20]. This accompanies the generation and storage of a greater dislocation density than that from quasi-static deformation processes. It is of interest to study the magnitude and spatial distribution of dislocation density under μLSP. Within the formalisms of the kinematical scattering of X-rays and the linear elasticity theory of dislocations, the modified Warren–Averbach method was used to evaluate the dislocation density from the X-ray profile analysis [16]. According to Eq. (3), nonlinear curve fitting with the least-squares evaluation was applied to the plot of the Fourier coefficients ln(A_n) versus n (Fig. 6). All six parameters c_0, ρ^*, Q^*R_e, R_2, and R_3 were calculated through six curve fitting parameters $P1-P6$. After obtaining the formal dislocation density ρ^*, the estimated true values of dislocation density are calculated by Eq. (4). Figure 7 shows the dislocation density across the shock line. As seen, the highest density occurs at the shock line center and decays slowly to the outer edge. The result is again consistent with the strain deviation result.

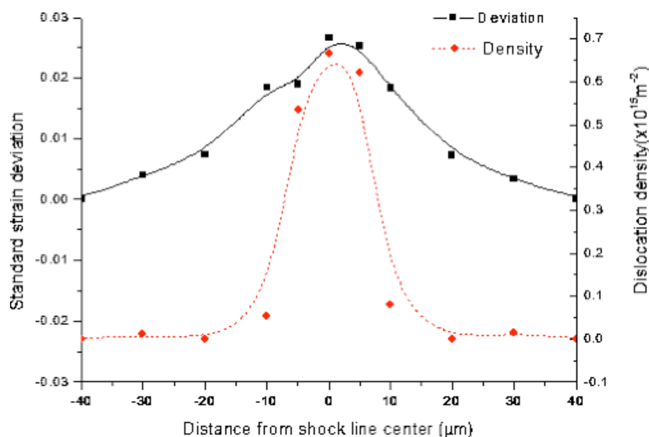

Fig. 7 Standard strain deviation in depth direction and dislocation density by Fourier transformation for the 3 μm copper thin film

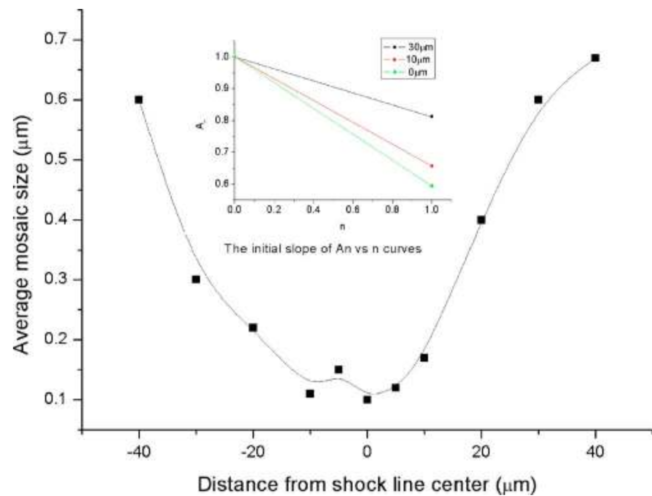

Fig. 8 Spatial distribution of average mosaic size based on FFT analysis of the initial slopes of the A_n versus n curves (as shown in the small figure) for 3 μm copper thin film

As discussed before, the size broadening effect is represented by a cosine Fourier series similar to that developed for strain broadening and hence the Fourier coefficients A_n give a very general method of handling either effect. From the analysis of Ref. [17], the initial slope of the A_n versus n curve is $(dA_n/dn)_{(n=0)}=-1/\bar{N}_3$, where $\bar{N}_3 a_3$ is the average column length and hence an average grain size in the direction a_3. So if the size broadening effect is expressed in terms of a plot of the Fourier coefficients A_n versus n, the initial slope of the curve gives directly the average column length, which is the average grain size in that direction. If the initial slope of curve is K, then the average grain size D at that position can be evaluated as $D=(1/K)\cdot a_3$. From the analysis above, the size effect can be obtained from Fourier analysis of X-ray profiles. Figure 8 shows the spatial distribution of average grain size evaluated from the X-ray profile analysis mention above. It can be seen that the average grain size decreases near to the shock line center. In the region of ±20 μm from the center, the grain size is around 0.1–0.2 μm. Therefore, the shocked area is strengthened due to a mosaic size refinement, according to the well-known empirical Hall–Petch relation [21].

4.2 Characterization of Silicon Substrate via X-Ray Microdiffraction Analysis. For the substrate silicon (bare Si), the shocked line is along the [110] direction because this condition may result in a predominately plane deformation state in (110) plane as shown in Ref. [9] for aluminum and copper. It was found that the X-ray profile for silicon (004) after μLSP is shifted to a higher angle and there is almost no broadening, that is, μLSP results in almost uniform and elastic strain in normal direction of the substrate. By using Bragg law $\Delta d/d=-\cot\theta\Delta\theta$, the strain distribution in normal direction is obtained and shown in Fig. 9. It can be seen that the affected region of μLSP for the substrate is about ±20 μm, which is the same as that for thin film at both laser energy levels. It is also consistent with the result by diffraction intensity contrast, which is shown in Fig. 10. Figure 9 shows that the maximum strain in normal direction induced by μLSP is below 0.05%, which means that μLSP with these two laser energy levels has little effect on the silicon substrate. Intensity contrast of

Downloaded 04 Jan 2008 to 128.59.149.201. Redistribution subject to ASME license or copyright; see http://www.asme.org/terms/Terms_Use.cfm

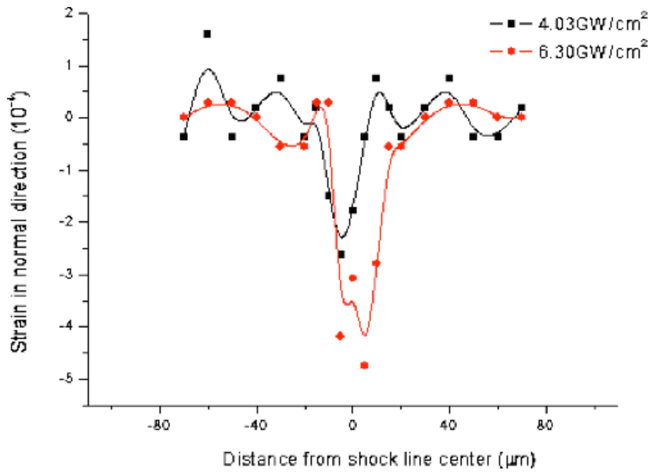

Fig. 9 Spatial distribution of strain normal to the irradiated surface of (004) single-crystal silicon based on X-ray diffraction measurements

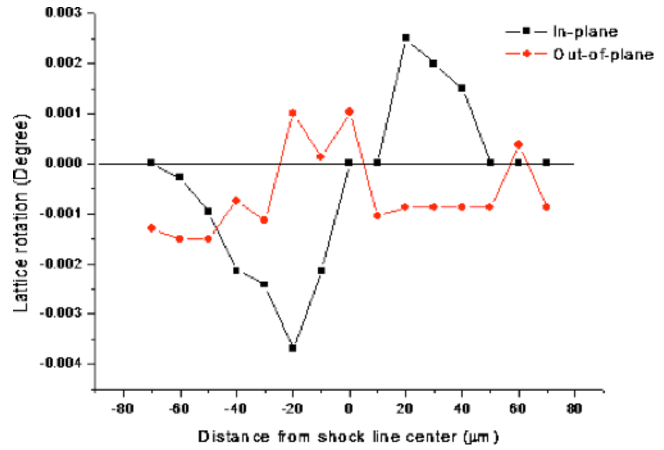

Fig. 11 In-plane and out-of-plane lattice rotation on shock peened surface of single-crystal silicon for 4.03 GW/cm² laser energy (obtained from the θ and χ scans, respectively, shown in Fig. 3)

the substrate with film is bigger than that without film, i.e., 1.9 (Fig. 4) with film and only 1.2 without film for laser energy 6.30 GW/cm^2. This is because the plastic deformation of film after μLSP,which is coupled to the substrate, is much more severe than that of bare silicon.

As mentioned in Sec. 3.1, two rotations, θ scan and χ scan were applied in the X-ray diffraction experiment to minimize the divergence effect (Fig. 3). The θ scan ensures that the mean beam vector of incident X-ray is at the proper angle with respect to the surface. The χ scan ensures that the normal vector of the diffracting plane is contained in the same geometrical plane as the incoming and diffracted X-ray beams. These two scans applied iteratively optimize the integrated intensity of the relevant reflection during alignment. Therefore, the in-plane and out-of-plane lattice rotation can be obtained from the θ and χ, scans, respectively. From Fig. 11, it is clear that the spatial distribution of in-plane lattice rotation in the substrate (004) is anti-symmetric with respect to the center of shock line. The maximum rotation angle is around ±0.003 deg at a position nearly ±20 μm away from the center of the shock line, while the variation of out-of-plane lattice rotation in Fig. 11 is only ±0.001 deg and quite small relative to in-plane lattice rotation since it is already approaching the resolution of the two Euler angles, which is 0.001 deg. The lattice rotation measurements confirm that the deformation is predominantly plane and symmetric about the shocked line center.

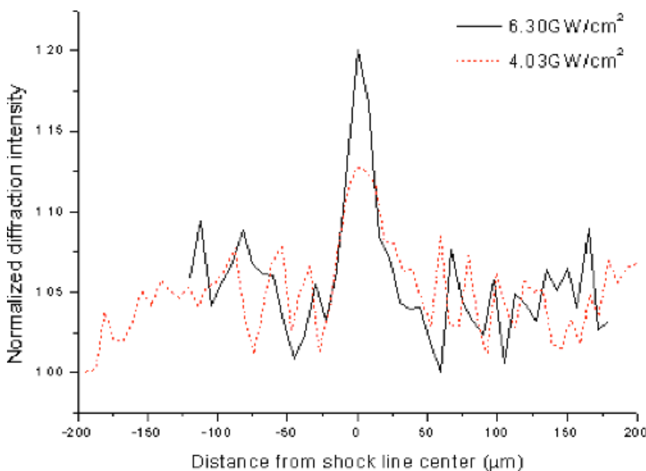

Fig. 10 Diffraction intensity contrast measurements across the shock line of (004) single-crystal silicon

4.3 Microstructure Characterization by EBSD Measurement

4.3.1 Crystallographic Texture. The physical properties of thin-film samples are dependent on the crystallographic texture, which can be easily identified from pole figures or inverse pole figures via EBSD [18]. In order to determine the texture precisely, the scanning area is set as large as possible, i.e., 20 μm $\times 20$ μm since the affected width is about 25 μm according to the X-ray microdiffraction results, and a step size of 0.5 μm was employed. From the inverse pole figure of the unshocked 1 μm film as shown in Fig. 12(*a*), it is clear that there is very strong (111) texture and relatively weak (001) texture, which is in accordance with the result of conventional X-ray diffraction shown in Fig. 2. After μLSP, the corresponding inverse pole figure is shown in Fig. 12(*b*). It can be found that the (111) texture intensity is weakened, while (001) texture intensity is enhanced. This change can be quantitatively analyzed through misorientation angle distribution of the ⟨001⟩ direction, which is relative to the surface normal to the sample. Intensities close to 0 deg correspond to the density of (001) texture while intensities around 54.7 deg are for (111) texture. It can be seen that the maximum intensity at low angles is doubled after LSP while the intensities around angle 54.7 deg somewhat decrease (see Fig. 13).

The change from the (111) deformation texture to the (001) recrystallization texture in room temperature could be explained by using the strain energy release maximization (SERM) model [22]. If a small volume of a uniaxially stressed material with fixed ends is replaced by the same volume of unstressed body, the strain energy of the system including the substituted region will be reduced. The released energy depends on Young's modulus of the substituted body and will be maximized if the substituted body has the texture which has the smallest Young's modulus. For the copper, Young's modulus are 66.7 GPa in ⟨100⟩ direction, 191.1 GPa in ⟨111⟩ direction, and 130 GPa in ⟨110⟩ direction. The minimum elastic modulus direction of copper thin film is the ⟨100⟩ direction. Therefore, the plastically deformed film having the (111) texture will have the (001) texture after recrystallization, which is in agreement with the measured results.

4.3.2 Grain Size and Subgrain Structures. Grain boundaries were distinguished by defining the corresponding misorientation angles and the grain size distribution of the sample were found using the EBSD post-processing software. In this case, the mis-

Downloaded 04 Jan 2008 to 128.59.149.201. Redistribution subject to ASME license or copyright; see http://www.asme.org/terms/Terms_Use.cfm

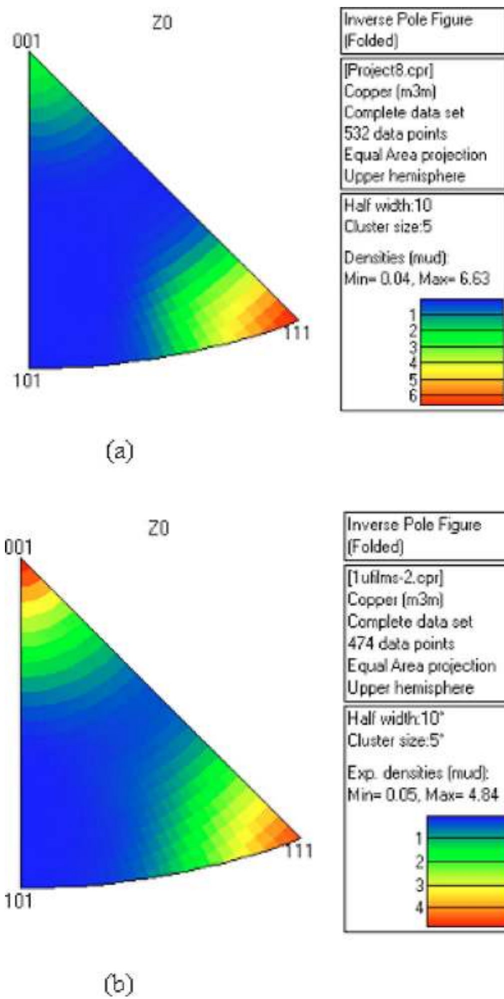

Fig. 12 Texture of 1 μm thin film by inverse pole figure: (*a*) raw sample; and (*b*) shocked area

orientation angle of grain boundary is set to be 10 deg, which is suitable for most materials. Because the grain diameter is likely the order of film thickness, a scanning area of 8 μm $\times$ 8 μm and step size of 0.1 μm were used. The maps of grain size before and after μLSP are shown in Fig. 14, in which the thick lines are the

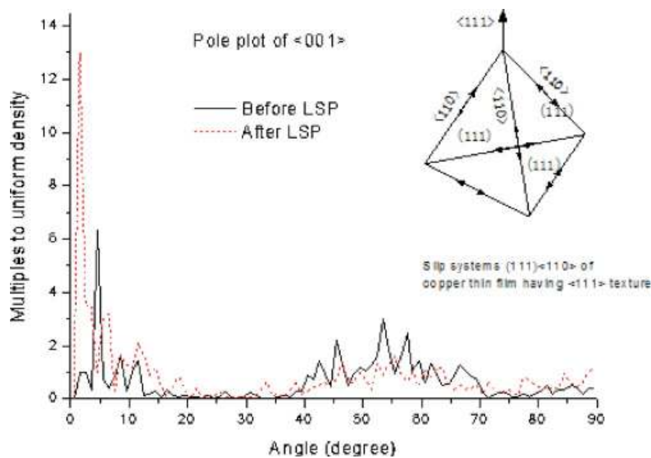

Fig. 13 Misorientation angle distribution of {001} lattice direction before and after LSP for 1 μm thin film and slip systems (111)⟨110⟩ for (111) film texture

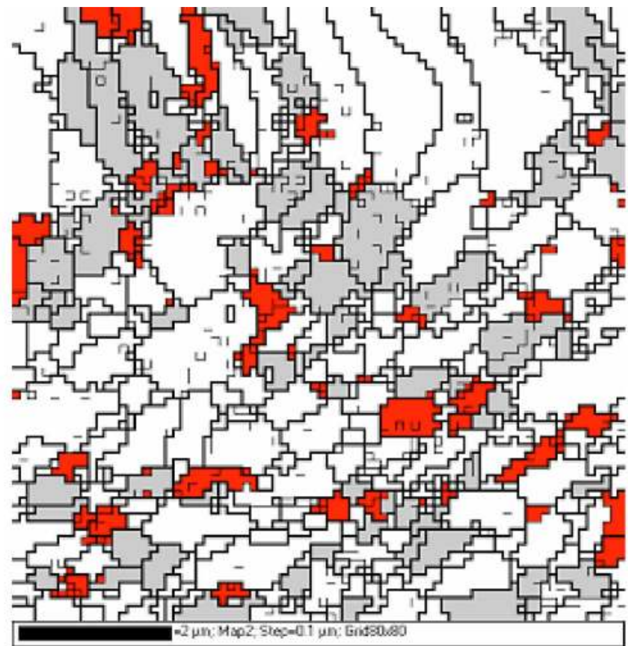

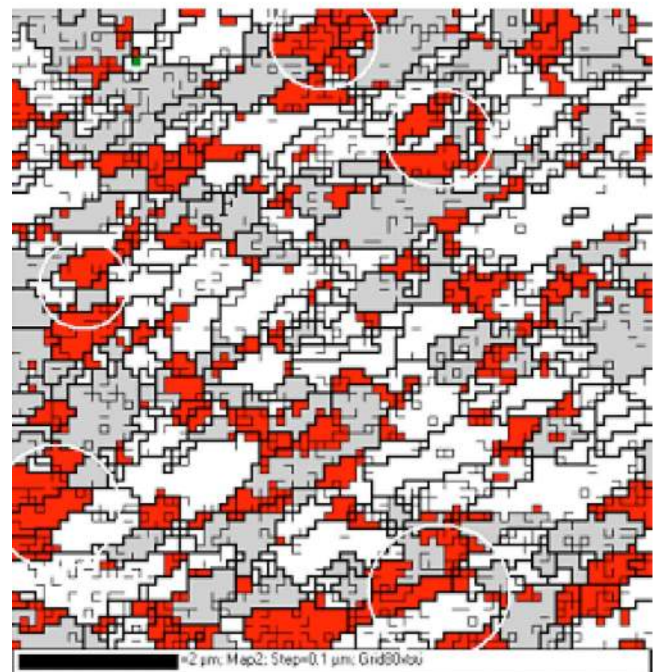

Fig. 14 Grain size map and subgrain structure changes through LSP of 1 μm thin film: (a) before LSP; (b) after LSP: red color: highly deformed region with the highest density of substructure, gray color: grains with medium density of substructures; white color: stress free grains that have less defects and substructures (circles shown in (b) are to be used with Fig. 17)

grain boundaries. By comparing Figs. 14(*a*) and 14(*b*), it is clear that after LSP the grain size becomes smaller and somewhat more uniform. The statistic results of Fig. 14 for distribution function of grain diameter as shown in Fig. 15 confirm that. This result is also in accordance with the result from atomic force microscopy

Downloaded 04 Jan 2008 to 128.59.149.201. Redistribution subject to ASME license or copyright; see http://www.asme.org/terms/Terms_Use.cfm

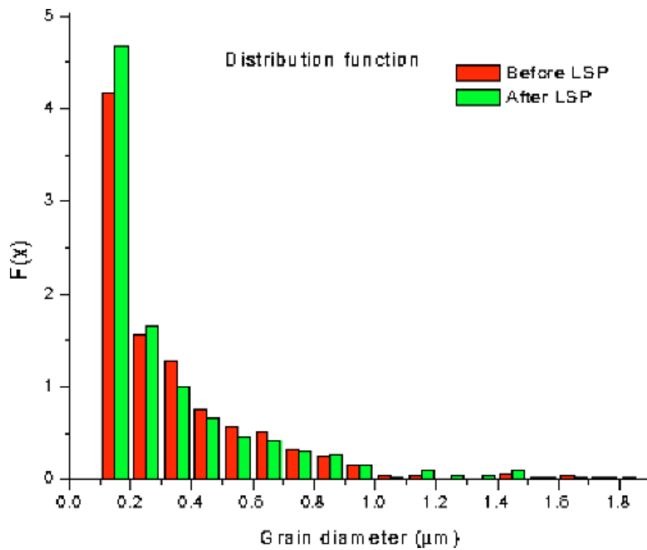

Fig. 15 Distribution of grain size for 1 μm thin film

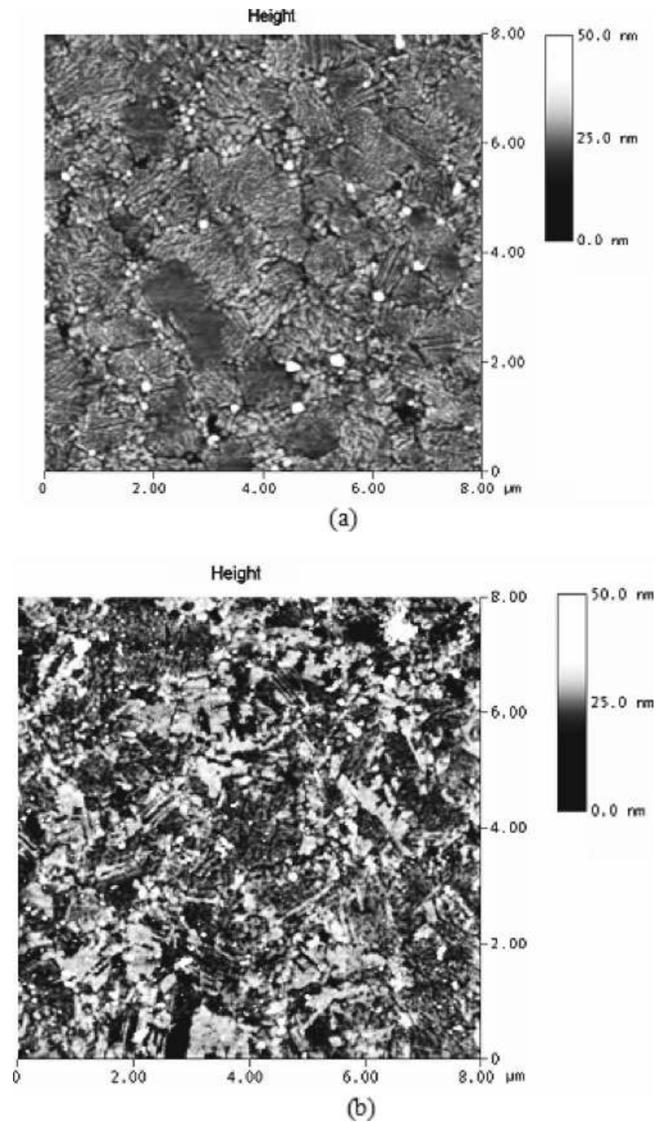

Fig. 16 Topography of 1 μm copper thin film by AFM: (*a*) raw thin film; (*b*) shocked film (scanning area 8 μm$\times$8 μm, data scale 2 μm)

(AFM) as shown in Fig. 16. Before LSP, the average diameter of grains is about 0.372 μm and the standard deviation is 0.375; after LSP, the average diameter of grains is about 0.302 μm and the standard deviation is 0.311. As a result of the grain size refinement, the shocked area is strengthened according to the well-known empirical relationship such as the Hall–Petch relation between average grain size and the yielding limit [21]. Also, the more uniform distribution of grain size results in higher yield strength compared with the material with a more scattered grain size distribution, because plastic strain is unevenly distributed among grains of different sizes [23] and uniform grain size tends to share the external load more uniformly and is desirable for neutralizing weak spots and thus stress concentration.

Besides using EBSD to investigate grain structure and crystallographic orientation, subgrain structures can also be quantitatively analyzed through EBSD measurements because of their high spatial and angular resolution, such as $\sim$25 nm and $\sim$0.8 deg for the W-filament SEM, respectively. The thinner lines in Figs. 14(*a*) and 14(*b*) show the subgrain boundaries, whose misorientation angles are larger than 1 deg, of the 1 μm copper film without and with LSP, respectively. The red area stands for highly deformed grains, which have the highest density of substructures such as twins and dislocations; the silver area stands for grains with substantial substructures; and the white area is the stress free grains that have less defects and substructures. Comparing these two maps, it is observed that there is a great increase in substructure and in the highly deformed region after LSP. Table 1 summarizes such changes.

The substructure changes due to LSP are characterized by high strain rate and higher uniformity as compared to normal deformation processes such as cold rolling. The shock front serves as subgrain structure (dislocation) sources when the shock pressure is higher than the critical shear stress. According to Ref. [24], dislocations are homogeneously nucleated at (or close to) the shock front by the deviatoric stresses set up by the shock load, and the generation of these dislocations relaxes the deviatoric stresses. These dislocations move short distances at subsonic speeds, and new dislocation interfaces are generated as the shock wave propagates through the material. When the shock pressure becomes less than the critical stress, substructure and plastic deformation growth halts. It can also be found that most of highly deformed regions (Fig. 14(*b*)) correspond to the (001) texture component as shown in Fig. 17, indicated by corresponding circles. This can be explained by Schmid's law. For face-center cubic (fcc) crystal, it is well known that the plastic slip systems are the (111) planes in the $\langle 110 \rangle$ directions, for a total of 12 possible slip systems. For the (111) orientation grains, there are six possible activated slip systems with Schmid's factor $-(2/3\sqrt{6})$: $(\bar{1}1\bar{1})[110]$, $(\bar{1}1\bar{1})[011]$, $(1\bar{1}\bar{1})[110]$, $(1\bar{1}\bar{1})[101]$, $(\bar{1}\bar{1}1)[011]$, and $(\bar{1}\bar{1}1)[101]$. For the (001) orientation, there are eight possible activated slip systems with Schmid's factor $\pm 1/\sqrt{6}$: $(111)[10\bar{1}]$, $(111)[1\bar{1}0]$, $(\bar{1}1\bar{1})[10\bar{1}]$, $(\bar{1}1\bar{1})[110]$, $(1\bar{1}\bar{1})[110]$, $(1\bar{1}\bar{1})[101]$, $(\bar{1}\bar{1}1)[101]$, and $(\bar{1}\bar{1}1)[1\bar{1}0]$, As a result, it is more difficult to deform in the

Table 1 Microstructure changes of 1 μm copper thin film after LSP

Area percentage	Before μLSP (%)	After μLSP (%)
Stress-free	57.8	42.6
With substructure	24.7	29.5
Highly deformed	17.5	27.9

Downloaded 04 Jan 2008 to 128.59.149.201. Redistribution subject to ASME license or copyright; see http://www.asme.org/terms/Terms_Use.cfm

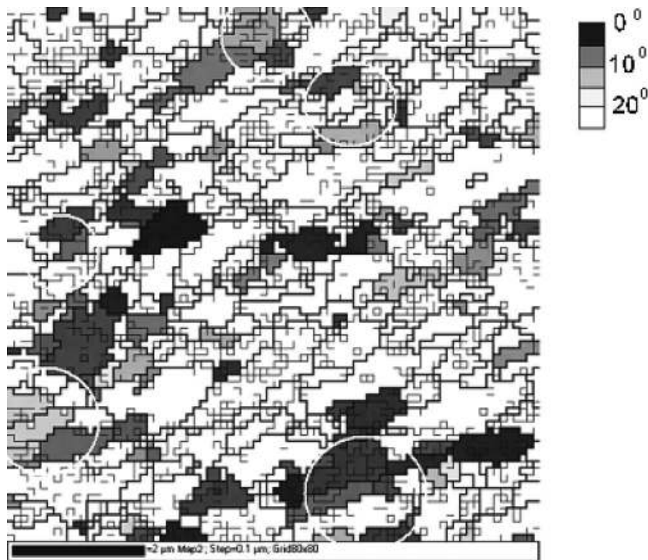

Fig. 17 (001) texture component corresponding to Fig. 16(*b*), the darker, the closer to the ⟨001⟩ direction; white regions are greater than 20 deg

(111) orientation compared with the (001) orientation.

The substantial increase of substructures is the major cause of strength and hardness improvement in LSP. With the increase of substructures, the subgrain size decreases, which has an effect similar to grain refinement. According to Ref. [20], the flow stress

$$\sigma = \sigma_0 + k_1 D^{-1/2} + k_2 d^{-1} \tag{6}$$

where σ_0, k_1, and k_2 are material constants; D is grain size; and d is the subgrain size. As a result, the yield strength of copper thin film increases after LSP. Both the compressive surface residual stress and the refined microstructure in LSP contribute to the fatigue life improvement.

4.4 FEM Simulation for the Silicon Substrate

4.4.1 Simulation Condition. The above results show that, although the copper films underwent appreciable plastic deformation under μLSP, the Si substrate understandably deforms very little. It is probable that the substrate can be treated linear elastic in modeling μLSP of thin films. To provide further evidence, the (004) Si substrate is numerically modeled and analyzed by assuming shock is applied directly on the substrate. The simulation is based on the theory of single-crystal plasticity to be briefly explained in the following paragraph. Although Si has a diamond cubic structure, it is assumed that silicon has a similar deformation mechanism to fcc metals for the following reasons [25]: (1) Diamond structure is similar to the fcc structure. The major difference is that diamond structure has four additional atoms in a unit cell. The (111) plane of a diamond structure is the most dense plane just like fcc metals and expected to slip similarly as fcc metals, especially when dislocation density is low such that glide dislocations lie primarily along ⟨110⟩ directions. (2) Its plastic behavior is reportedly similar to fcc metals though it can only deform slightly at room temperature [26].

Based on the theory of single-crystal plasticity [27], a user-material subroutine termed UMAT for single-crystal plasticity written by Huang [28] and modified by Kysar [29] is incorporated into the finite-element program ABAQUS [30]. Crystal shear stress of 1 GPa on each slip system is assumed [25]. The temporal dependent shock pressure was modeled by using mass, momentum, and energy conservation in axial direction and solved numerically [10]. The pressure was then extended to a nonuniform shock profile with a Gaussian spatial distribution [10] since the beam spot size is relatively small and applied as the loading of the subsequent FEM analysis for the substrate. Simulation was carried out assuming finite geometry (800 μm in length and 400 μm in height). The bottom surface is fixed in position, while all the other side surfaces are set traction free.

The induced deformation state is two dimensional, i.e., a plane stress deformation state [9] and this point has been explained early in the paper as well. Also, strain rate and hardening effects are ignored in simulation due to the absence of constitutive data in this region. By using this simplified simulation model, the goal is to understand the overall character of the induced deformation and see how much can be predicted. Furthermore, it is hoped that these simulations will lay the groundwork for more realistic simulations of thin film with substrate.

4.4.2 Simulation Results and Discussion. Figure 18(*a*) shows the contour of strain distribution in the normal direction for laser energy 4.03 GW/cm^2. In order to compare to the result from X-ray measurement, the in-depth strain is averaged over the effective penetration distance of the X-ray. For θ-2θ diffraction configuration, the effective penetration depth is

$$x = \frac{K_x \sin(\theta)}{2\mu} \tag{7}$$

where μ is the X-ray absorption coefficient of the sample and K_x corresponds to the percentage of absorption [15]. For the wavelength of $\lambda = 1.458$ Å, μ of the silicon substrate is about 152.2. Considering 90% absorption, the effective penetration depth can be calculated to be 42 μm. By averaging strains in depth to 42 μm, we can find the strain component in the normal direction, which is comparable with the result from the X-ray (Fig. 18(*b*)).

Figure 19(*a*) shows the contour of the lattice rotation field of the (004) silicon substrate from simulation. Averaging the lattice rotation in Fig. 19(*a*) in the depth of X-ray penetration, we can compare the simulation result to that of X-ray measurement as shown in Fig. 19(*b*). They show a similar trend but the FEM result is larger than that from the X-ray. Perhaps it is due to the fact that the diamond structure of Si is approximated by fcc in FEM and the latter is easier to deform.

Single-crystal silicon deforms plastically in an anisotropic manner. In this case, the deformation occurs by the creation and motion of dislocation within the crystal on discrete slip systems under the assumption of plane strain conditions. It is then of interest to study plastic slips in each activated slip system which satisfies this assumption. According to Ref. [31], there are three pairs of effective slip systems that satisfy this assumption if a line loading is in the direction of ⟨110⟩ direction as shown in Fig. 20. There are slip system i, combination of slip systems $(1\bar{1}1)[011]$ and $(1\bar{1}1)[10\bar{1}]$, slip system ii, combination of slip systems $(\bar{1}11)\times[101]$ and $(\bar{1}11)[0\bar{1}1]$, and complex slip system iii, combination of slip systems $(111)[\bar{1}10]$ and $(11\bar{1})[\bar{1}10]$. When activated in equal amounts, the corresponding two slip systems can combine to form an effective slip system as just mentioned, which act in the (110) plane. Thus, the shock loading generates a predominately plane deformation state in the (110) plane if shocking is along the [110] direction.

Figures 21(*a*)–21(*d*) shows the predicted plastic shear strain on each slip system, as well as total accumulated plastic shear strain summed over all slip systems. From Figs. 21(*a*)–21(*d*), slip systems i and ii have the same shear strain distribution because of symmetry. Shear strain in slip system iii shown in Fig. 21(*c*) is much smaller than others because its Schmid's factor is zero. It can be seen that the total shear strain is the sum of the shear strains of the three slip systems, which means other slip systems are not activated and is in accordance with the assumption of plane strain deformation. As seen, the slip systems i and ii are active from a distance to the surface, which can be explained by

Downloaded 04 Jan 2008 to 128.59.149.201. Redistribution subject to ASME license or copyright; see http://www.asme.org/terms/Terms_Use.cfm

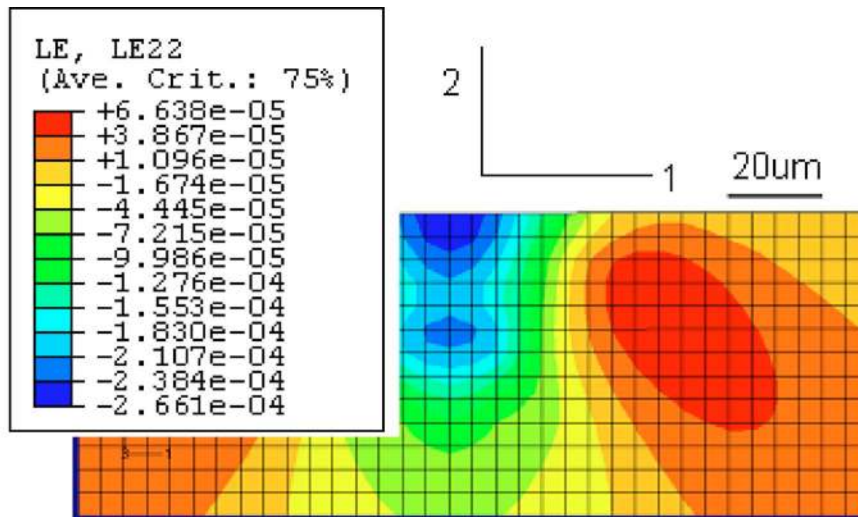

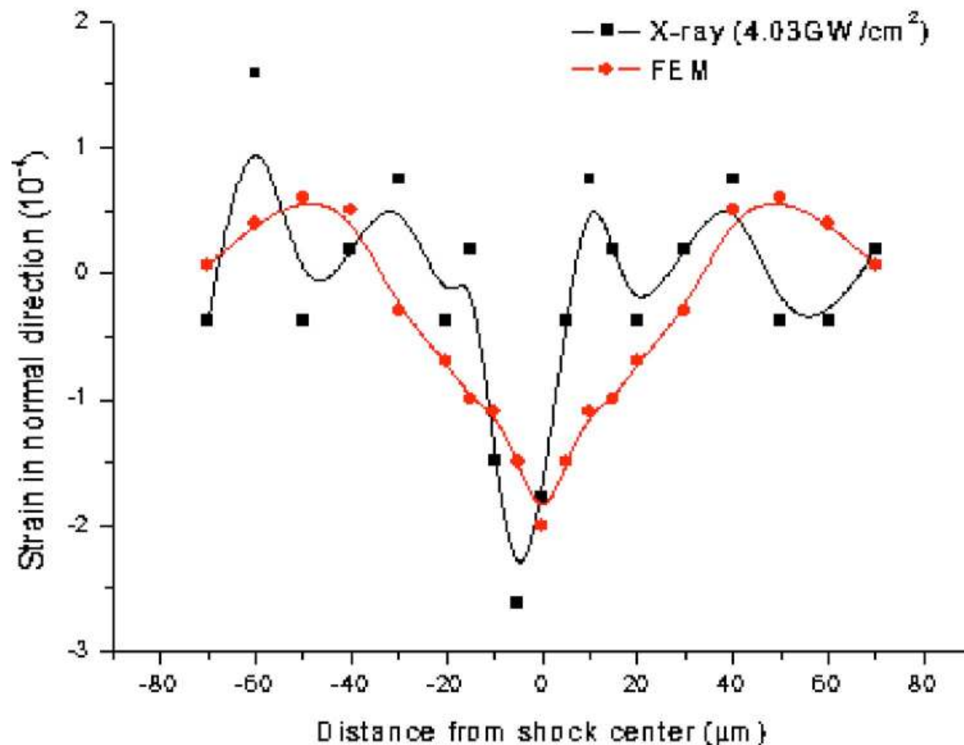

Fig. 18 Strain normal to the irradiated top surface for single crystal silicon: (*a*) strain distribution by FEM; and (*b*) comparison between FEM and X-ray results

the distribution of the corresponding resolved shear stress in each slip system. Extracting normal stress σ_{22}, stress σ_{11} tangent to the top surface, and the corresponding shear stress σ_{12}, the corresponding resolved shear stress in an inclined plane is

$$\sigma'_{12} = \frac{\sigma_{22} - \sigma_{11}}{2} \sin 2\theta + \sigma_{12} \cos 2\theta \tag{8}$$

where θ is the angle between the inclined plane and direction 1 as indicated in Fig. 21. For slip system i, ii, θ is -54.7 deg and 54.7 deg, respectively. Based on the above equation, the contours of resolved shear stress in slip systems i and ii are calculated and shown in Fig. 22. It is seen that the plastic shear strain region (Figs. 21(*a*) and 21(*b*)) matches that of the maximum resolved shear stress in the corresponding slip system (Figs. 22(*a*) and 22(*b*)). The maximum resolved shear stress is about 1.051 GPa, just above the critical shear stress of 1 GPa set for the simulation. In summary, little plastic deformation was induced by μLSP as evidenced here again in Figs. 21(*a*) and 21(*b*). The maximal shear strain is only 0.04% and thus the Si substrate may be treated as linear elastic as far as μLSP applied to thin films is concerned.

Downloaded 04 Jan 2008 to 128.59.149.201. Redistribution subject to ASME license or copyright; see http://www.asme.org/terms/Terms_Use.cfm

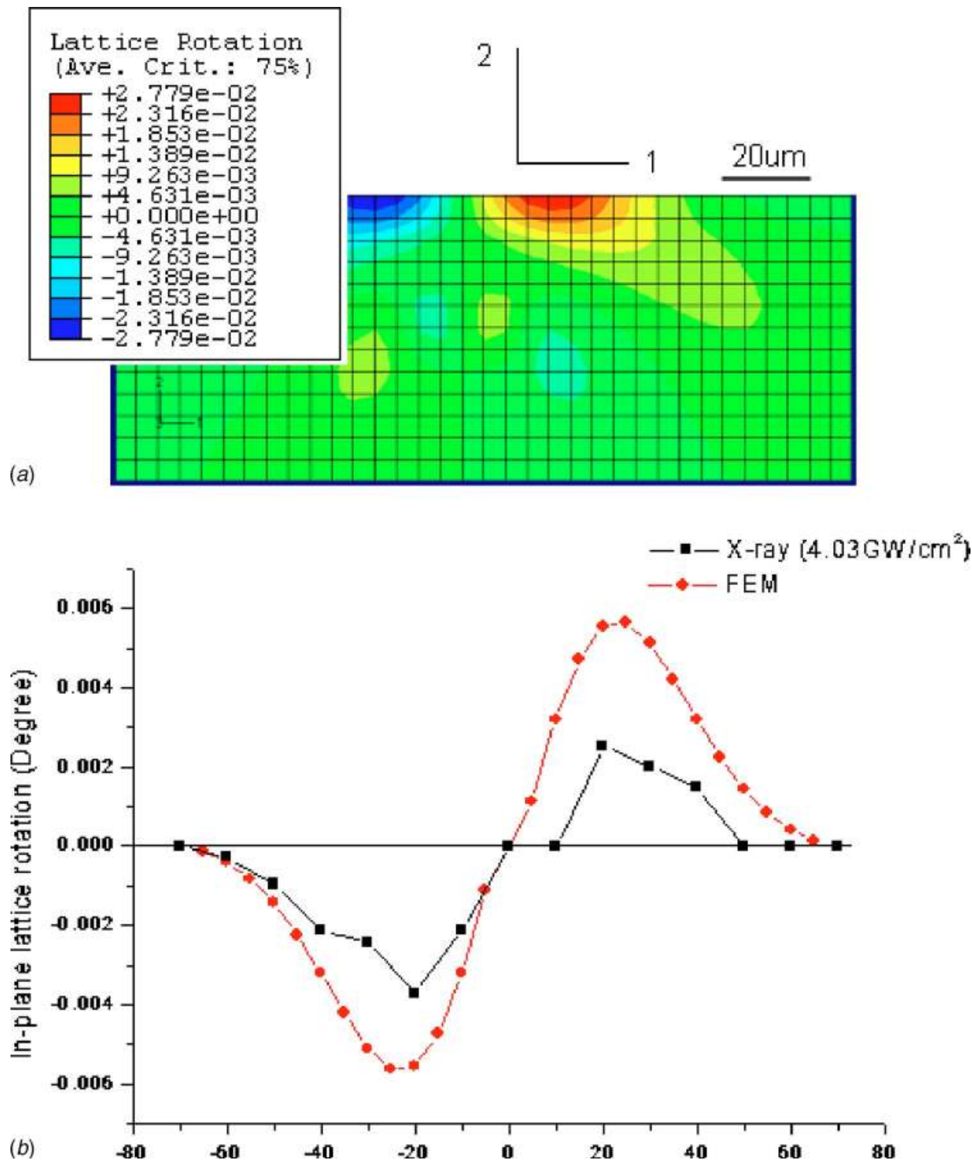

Fig. 19 In-plane lattice rotation for single-crystal silicon: (*a*) lattice rotation distribution by FEM; and (*b*) comparison of FEM and X-ray results

5 Conclusions

In this paper, shock peened copper thin films on (004) single silicon substrate were characterized using microdiffraction X-ray and EBSD. The induced stress/strain on film and substrate was estimated, which indicates that the affected cross-section area, perpendicular to shock line, is about ± 20 μm for a 12-μm-diameter laser spot size. The strain deviation of ± 0.025 and dislocation density of 0.7×10^{15} m^{-2} strongly indicate that the nonuniform plastic deformation is induced by μLSP as in bulk metals. Also, microstructure of 1 μm films after μLSP was quantified by using EBSD. It was seen that the strong texture (111) was compromised by (001) texture, which can be well understood through the SERM model. In addition, the distribution of grain size after μLSP becomes more uniform and smaller, shown by the results from X-ray diffraction, AFM, and EBSD measurements. Both the above trends result in the increase of yield strength of the shock peened area, as well as hardness. Besides that, EBSD measurement also shows the increase of subgrain structures that was quantified and used to help explain the fatigue performance improvement by μLSP. To shed some light on the role of the silicon substrate, it was investigated experimentally and via simulation. From experimental results of the diffraction intensity contrast, strain distribution, and lattice rotation, it is clear that the silicon substrate experiences little plastic deformation compared with that of metal films, which is in good agreement with the results from the FEM simulation. The results were further explored and explained in terms of plastic shear strain and corresponding stress in

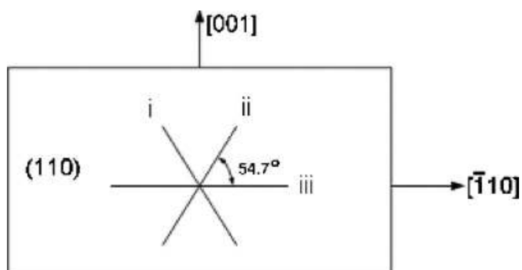

Fig. 20 Plane strain slip systems for (001) single crystal sample

Downloaded 04 Jan 2008 to 128.59.149.201. Redistribution subject to ASME license or copyright; see http://www.asme.org/terms/Terms_Use.cfm

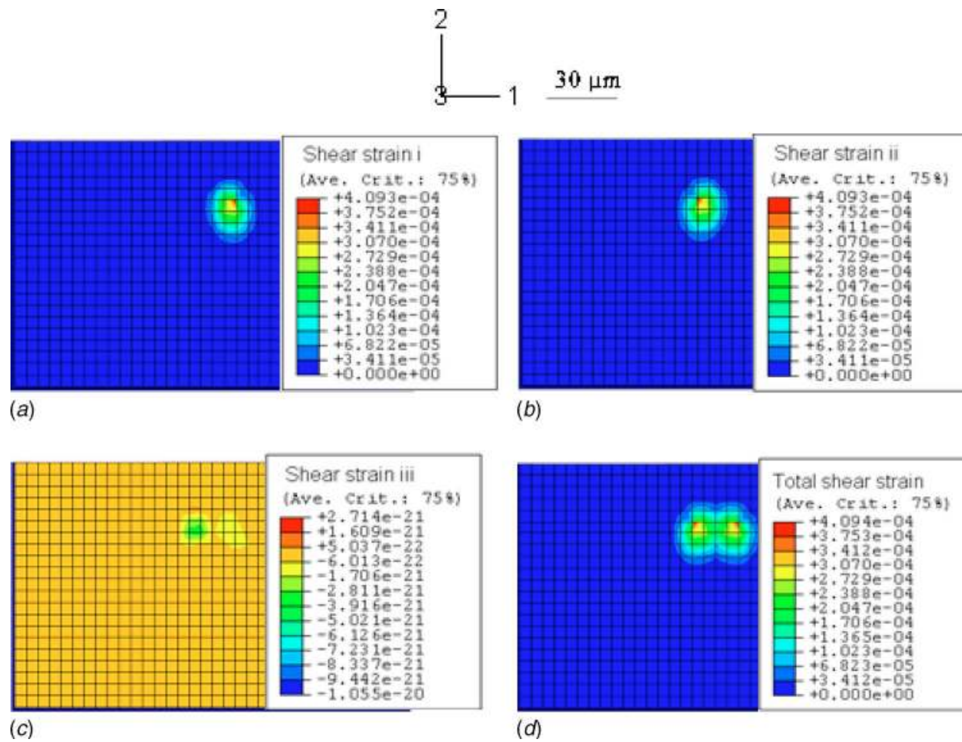

Fig. 21 (*a*) **Plastic shear strain for slip system i;** (*b*) **plastic shear strain for slip system ii;** (*c*) **plastic shear strain for slip system iii; and** (*d*) **total plastic shear strain (total simulation region is 800** μ**m** $\times$ **400** μ**m)**

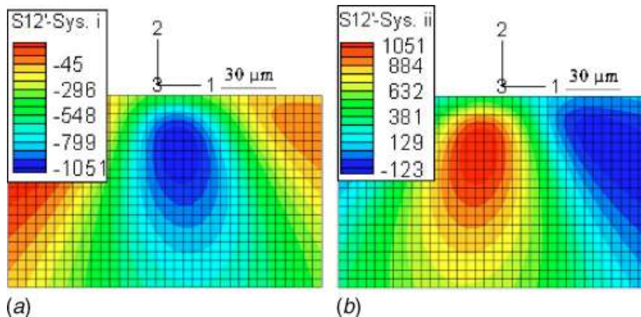

Fig. 22 Resolved shear stress contour in: (*a*) **slip system i;** (*b*) **slip system ii (corresponding to Figs. 21(*a*) and 21(*b*), respectively, unit is MPa)**

active slip systems. It appears that the Si substrate can be treated as linear elastic as far as μLSP on thin films is concerned.

Acknowledgment

Support from NSF Grant No. DMI-02-00334, NSF Grant No. CMS-0134226, and AFOSR Grant No. FA5550-06-1-0214 is gratefully acknowledged. Also, the work was supported in part by MRSEC Program of the National Science Foundation under Award No. DMR-0213574 and by the New York State Office of Science, Technology and Academic Research (NYSTAR). Dr. I. Cev Noyan and Dr. Jean Jordan-Sweet of IBM Watson Research Center provided valuable guidance and assistance at the National Synchrotron Light Source at Brookhaven National Laboratory. Assistance in technical details for EBSD provided by Mr. Paul Van Der Wilt is also acknowledged.

References

[1] Spengen, W. M., 2003, "MEMS Reliability from a Failure Mechanisms Perspective," Microelectron. Reliab., **43**, pp. 1049–1060.

[2] Stark, B., 1999, *MEMS Reliability Assurance Guidelines for Space Applications*, National Aeronautics and Space Administration (NASA) and Jet Propulsion Laboratory (JPL), California Institute of Technology, Pasadena, CA.

[3] Wang, W., Wang, Y., Bao, H., Xiong, B., and Bao, M., 2002, "Friction and Wear Properties in MEMS," Sens. Actuators, A, **97–98**, pp. 486–491.

[4] Clauer, A. H., and Holbrook, J. H., 1981, "Effects of Laser Induced Shock Waves on Metals," *Shock Waves and High Strain Phenomena in Metals-Concepts and Applications*, Plenum, New York, pp. 675–702.

[5] Clauer, A. H., and Lahrman, D. F., 2001, "Laser Shock Processing as a Surface Enhancement Process," Key Eng. Mater., **197**, pp. 121–142.

[6] Gomez-Rosas, G., Rubio-Gonzalez, C., Ocana, J. L., Molpeceres, C., Porro, J. A., Chi-Moreno, W., and Morales, M., 2005, "High Level Compressive Residual Stresses Produced in Aluminum Alloys by Laser Shock Processing," Appl. Surf. Sci., **252**, pp. 883–887.

[7] Sanchez-Santana, U., Rubio-Gonzalez, C., Gomez-Rosas, G., Ocana, J. L., Molpeceres, C., Porro, J., and Morales, M., 2006, "Wear and Friction of 6061-T6 Aluminum Alloy Treated by Laser Shock Processing," Wear, **260**, pp. 847–854.

[8] Zhang, W., and Yao, Y. L., 2001, "Feasibility Study of Inducing Desirable Residual Stress Distribution in Laser Micromachining," *Transactions of the North American Manufacturing Research Institution of SME (NAMRC 29th) 2001*, Gainesville, FL, pp. 413–420.

[9] Chen, H. Q., Kysar, J. W., and Yao, Y. L., 2004, "Characterization of Plastic Deformation Induced by Micro Scale Laser Shock Peening," ASME J. Appl. Mech., **71**, pp. 713–723.

[10] Zhang, W., Yao, Y. L., and Noyan, I. C., 2004, "Microscale Laser Shock Peening of Thin Films, Part 1: Experiment, Modeling and Simulation," J. Manuf. Sci. Eng., **126**, pp. 10–17.

[11] Zhang, W., Yao, Y. L., and Noyan, I. C., 2004, "Microscale Laser Shock Peening of Thin Films, Part 2: High Spatial Resolution Material Characterization," J. Manuf. Sci. Eng., **126**, pp. 18–24.

[12] Fox, J. A., 1974, "Effect of Water and Paint Coatings on Laser-Irradiated Targets," Appl. Phys. Lett., **24**(10), pp. 461–464.

[13] Noyan, I. C., Jordan-Sweet, J. L., Liniger, E. G., and Kaldor, S. K., 1998, "Characterization of Substrate/Thin-Film Interfaces With X-Ray Microdiffraction," Appl. Phys. Lett., **72**(25), pp. 3338–3340.

[14] Zhang, W., and Yao, Y. L., 2000, "Micro Scale Laser Shock Processing of Metallic Components," J. Manuf. Sci. Eng., **124**(2), pp. 369–378.

[15] Cullity, B. D., 1978, *Elements of X-Ray Diffraction*, 2nd ed., Addison-Wesley Publishing Company, Inc., London, pp. 268–270.

[16] Ungar, T., and Borbely, A., 1996, "The Effect of Dislocation Contrast on X-Ray Line Broadening: A New Approach to Line Profile Analysis," Appl. Phys. Lett., **69**, pp. 3173–3175.

[17] Warren, B. E., and Averbach, B. L., 1950, "The Effect of Cold-Work Distortion on X-Ray Patterns," J. Appl. Phys., **21**, pp. 595–599.

Downloaded 04 Jan 2008 to 128.59.149.201. Redistribution subject to ASME license or copyright; see http://www.asme.org/terms/Terms_Use.cfm

[18] Adam, J. S., Kumar, M., and Adams, B. L., 2000, *Electron Backscatter Diffraction in Materials Science*, Kluwer Academic, New York.
[19] Noyan, I. C., and Cohen, J. B., 1987, *Residual Stress-Measurement by Diffraction and Interpretation*, Springer, New York pp. 168–175.
[20] Murr, L. E., 1981, "Residual Microstructure—Mechanical Property Relations in Shock-Loaded Metals and Alloys," *Shock Waves and High Strain Phenomena in Metals-Concepts and Applications*, Plenum, New York pp. 635–655.
[21] Hertzberg, R. W., 1995, *Deformation and Fracture Mechanics of Engineering Materials*, Wiley, New York.
[22] Lee, D. N., 2000, "Strain Energy Release Maximization Model for Evolution of Recrystallization Textures," Int. J. Mech. Sci., **42**, pp. 1645–1678.
[23] Novikov, V., 1997, *Grain Growth and Control of Microstructure and Texture in Polycrystalline Materials*, CRC, New York, pp. 11.
[24] Meyers, M. A., and Murr, L. E., 1981, *Shock Waves and High-Strain-Rate Phenomena in Metals*, Plenum, New York, pp. 487–530.
[25] Yoshino, M., Aoki, T., Chandrasekaran, N., Shirakashi, T., and Komanduri, R., 2001, "Finite Element Simulation of Plane Strain Plastic-Elastic Indentation on Single-Crystal Silicon," Int. J. Mech. Sci., **43**(2), pp. 313–333.
[26] Hill, M. J., and Rowcliffe, D. J., 1974, "Deformation of Silicon at Low Temperatures," J. Mater. Sci., **9**, pp. 1569–1576.
[27] Asaro, R. J., 1983, "Micromechanics of Crystals and Polycrystals," Adv. Appl. Mech., **23**, pp. 1–115.
[28] Huang, Y., 1991, "A User-Material Subroutine Incorporating Single Crystal Plasticity In the ABAQUS Finite Element Program," Mech Report No. 178, Division of Applied Sciences, Harvard University, Cambridge, MA.
[29] Kysar, J. W., 1997, Addendum to "A User- Material Subroutine Incorporating Single Crystal Plasticity In the ABAQUS Finite Element Program," Mech Report No. 178, Division of Engineering and Applied Sciences, Harvard University, Cambridge, MA.
[30] Hibbit, Karlsson and Sorensen, Inc., 2002, *ABAQUS/Standard User's Manual*, Version 6.2, Pawtucket, RI.
[31] Kysar, J. W., and Briant, C. L., 2002, "Crack Tip Deformation Fields In Ductile Single Crystals," Acta Mater., **50**, pp. 2367–2380.

Downloaded 04 Jan 2008 to 128.59.149.201. Redistribution subject to ASME license or copyright; see http://www.asme.org/terms/Terms_Use.cfm